Materials Today Bio 12 (2021) 100145

Contents lists available at ScienceDirect

Materials Today Bio

journal homepage: www.journals.elsevier.com/materials-today-bio

Liquid repellency enabled antipathogen coatings

W. Li [a,b,1], Y. Wang [c,d,e,1], X. Tang [a,b], T.T.T. Yuen [c,d,e], X. Han [a,b], J. Li [a,b], N. Huang [a], J.F.W. Chan [c,d,e], H. Chu [c,d,e,**], L. Wang [a,b,*]

[a] Department of Mechanical Engineering, The University of Hong Kong, Hong Kong
[b] HKU-Zhejiang Institute of Research and Innovation (HKU-ZIRI), Hangzhou, Zhejiang 311300, China
[c] State Key Laboratory of Emerging Infectious Diseases, The University of Hong Kong, Hong Kong
[d] Carol Yu Centre for Infection, The University of Hong Kong, Hong Kong
[e] Department of Microbiology, Li Ka Shing Faculty of Medicine, The University of Hong Kong, Hong Kong

ARTICLE INFO

Keywords:
SARS-CoV-2
Droplet
Antipathogen coating
Liquid/solid adhesion
Wettability

ABSTRACT

Currently, Coronavirus Disease 2019 (COVID-19)—a respiratory contagion spreading through expiratory droplets—has evolved into a global pandemic, severely impacting the public health. Importantly, the emerging of immune evasion SARS-CoV-2 variants and the limited effect of current antivirals against SARS-CoV-2 in clinical trials suggested that alternative strategies in addition to the conventional vaccines and antivirals are required to successfully control the COVID-19 pandemic. Here, we propose to use liquid-repellent coatings to prevent the spread of the disease in the absence of effective vaccines, antimicrobial agents, or therapeutics, wherein the deposition and penetration of pathogen droplets are prohibited. We use SARS-CoV-2 as a model pathogen and find that SARS-CoV-2 remnants are reduced by seven orders of magnitude on coated surfaces, yielding a repelling efficacy far outperforming the inactivation rate of disinfectants. The SARS-CoV-2 remnant scales exponentially with the liquid/solid adhesion, uncovering the mechanism and effective means for minimizing pathogen attachment. The antipathogen coating that both repels and inactivates pathogens is demonstrated by incorporating the super-liquid-repellent coating with antipathogen additives. Together with its versatility over a wide range of substrates and pathogens, the novel antipathogen coating is of considerable value for infection control in everyday life as well as during pandemics.

1. Introduction

Since its first report in December 2019, the extremely contagious Coronavirus Disease 2019 (COVID-19)—caused by severe acute respiratory syndrome coronavirus 2 (SARS-CoV-2)—has already inflicted over 200 million infections and more than 4 million deaths worldwide by August 2021 [1]. Importantly, recent clinical trial results suggested that the current antivirals used against COVID-19, including remdesivir and type I interferon, were of limited effects against the disease [2]. In addition, the emerging SARS-CoV-2 variants, including the B.1.351, P.1, as well as the more recent B.1.617 variants, contain key mutations at the receptor-binding domain of spike proteins that result in immune evasion [3–5]. These findings highlighted the importance of establishing alternative strategies to combat against the virus in addition to the conventional antivirals and vaccines. Pathogens like SARS-CoV-2 are transmitted through direct exposure to pathogen-laden droplets exhaled during talking, coughing, or sneezing [6,7]. Another potential route is the contact with "fomite", an infectious source generated after the landing pathogen droplets evaporate on surfaces such as those of food package, doorknob, lift button, and handrail [8–11]. For example, contaminated fomite plays a key role in spreading diarrheal pathogens such as rotavirus, *Escherichia coli* strains, and *Shigella* species [12–14]. As pathogens in dry nuclei can remain infectious for days on smooth surfaces and even for months at low temperatures [15,16], it is critical to minimize the attachment/deposition of pathogen-laden droplets on the surface [17–19].

Personal protective equipment such as surgical masks block the airborne route of transmission through filtration wherein a micro-/nanofiber matrix traps pathogens using inertial and electrostatic forces [20]. However, the filtering efficacy may be offset by the

* Corresponding author.
** Corresponding author.
E-mail addresses: hinchu@hku.hk (H. Chu), lqwang@hku.hk (L. Wang).
[1] These authors contributed equally to this work.

https://doi.org/10.1016/j.mtbio.2021.100145
Received 26 July 2021; Received in revised form 23 September 2021; Accepted 30 September 2021
Available online 7 October 2021

high-momentum cloud flow, a multiphase flow of 7–8 m with a velocity peaking at 10–30 m s^{-1} produced by sneezes and coughs carrying pathogen-laden droplets (~1–2000 μm in diameter) [21–23]. The insufficiency of current protective techniques is evidenced by a fact that ~6% of the infection cases are front-line medical workers [24]. In addition to proper fitting of face masks to protect medical workers [25], additional strategy to prohibit droplets retention on personal protective equipment and frequently touched surfaces yet remains absent from the current antipathogen toolbox [26].

Pinpointing the fluidic transmission nature, we propose to exploit a super liquid-repellent surface for the upgrading of personal protection as it prohibits liquid delivery and resists the high-momentum droplet impact [27–30]. Unlike masks which protect people from infection by filtration during respiration, or disinfectants that inactivate the pathogen after pathogen deposition, the super liquid-repellent surface minimizes pathogen attachment/deposition via directly repelling pathogen-containing droplets in the first place. For a superhydrophobic (SHP) surface, an aqueous droplet preferentially resides atop micro-/-nanotextures wherein the sparse liquid/solid contacts promote interfacial detachments [31–33]. By introducing re-entrant micro-/nanostructures and special low-surface-energy polymers, the surface can be made repellent to both water and oil, termed superamphiphobicity (SAP), or even nearly all types of liquids that include alcohol in addition to water and oil, termed superomniphobicity (SOP) [34–39]. Upon impact, liquid penetration attempt is thwarted by the nanoscopic porosity, building a shield toward the pathogen-bearing droplets [40]. By further incorporating antipathogen additives such as silver nanoparticles into the coating, the trace amount of residual pathogens could be further inactivated. Our preliminary study shows that a superhydrophobic surface demonstrates super-repellency to droplets loaded with SARS-CoV-2 [41]. However, the exact repelling efficacy of other liquid-repellent surfaces, including superamphiphobic and superomniphobic surfaces, against SARS-CoV-2 remains unexamined. Moreover, the antiviral efficacy of common metals, including silver and copper nanoparticles, toward SARS-CoV-2 remains unknown.

To study the repellent repertoire, we fabricate six types of nonwetting surfaces on a large materials gamut, including glass, fabric, steel, copper, mask, nitrile glove, and paper. We use SARS-CoV-2 as a model pathogen and find that they have super-repellency to droplets loaded with SARS-CoV-2. We trace the viral residue along the rolling trails of the droplets and find that SARS-CoV-2 remnants are reduced by seven orders of magnitude, a value that outperforms the inactivation rate of the disinfection procedure and the filtration efficiency of a mask. More importantly, we uncover that the amount of SARS-CoV-2 remnant grows exponentially with the increase in liquid/solid adhesion, capillary force parameterized by pinned fractions φ (depending on physical textures) and receding contact angles θ_{rec} (depending on the surface chemistry). Furthermore, silver nanoparticles are found to exhibit a remarkable anti-SARS-CoV-2 effect and the composite antipathogen coating is proposed by incorporating silver nanoparticles into super-liquid-repellent coatings. Such pathogen repelling strategy can be widely applied and would be effective for various pathogens such as bacteria and fungi in addition to viruses, thus being valuable for infection control in daily life as well as during epidemics. The antipathogen coating will also be useful in preventing the spread of disease in the absence of specific vaccines, antimicrobial agents, or therapeutics.

2. Materials and methods

2.1. Materials

1*H*,1*H*,2*H*,2*H*-perfluorodecyltrichlorosilane (PFDTS) (97%) was purchased from Gelest. 1*H*,1*H*,2*H*,2*H*-perfluorodecyltriethoxysilane (>98.0%) and tris(hydroxymethyl)aminomethane (>99.0%) were purchased from Tokyo Chemical Industry Corporation. 1*H*,1*H*,2*H*,2*H*-perfluorooctyltriethoxysilane (98%), 1*H*,1*H*,2*H*,2*H*-perfluorodecanethiol (97%), silver nitrate (≥99.0%), tetraethyl orthosilicate (TEOS) (≥99%), dichloromethane (≥99.5%), and fluorescein isothiocyanate (FITC)-BSA (FITC-BSA) were purchased from Sigma-Aldrich. Sodium hydroxide (97%) and potassium persulfate (≥99.0%) were purchased from J&K Scientific. Ammonium hydroxide (28–30% in water) and hydrochloric acid (37% in water) were purchased from Acros. Silica nanoparticles (15 nm) were purchased from Shanghai Maikun Chemical Co., Ltd., China. Titanium oxide nanoparticles (99.8%, anatase, ~100 nm) were purchased from Macklin. Nanosilver solution (1000 ppm in water) was purchased from Aladdin. A Sylgard 184 silicone elastomer kit was purchased from Dow Corning. Ethanol (absolute) was purchased from VWR International. Deionized water was produced using a deionized water system (DINEC, Hong Kong). Commercial glass slide, polyester fabrics, steel sheet, copper sheet, mask, nitrile gloves, and printing paper are cut into ~2 cm × 2 cm.

2.2. Virus adhesion test

SARS-CoV-2 HKU-001a was isolated from a nasopharyngeal aspirate specimen of a laboratory-confirmed COVID-19 patient in Hong Kong as we previously described [42]. The virus was suspended in Dulbecco's Modified Eagle Medium (DMEM) and was titered in VeroE6 cells with plaque assays as we previously described [43]. All experiments involving live SARS-CoV-2 followed the approved standard operating procedures of the Biosafety Level 3 facility at the Department of Microbiology, University of Hong Kong. The inactivated SARS-CoV-2 virus solution was prepared by incubating the virus in 4% paraformaldehyde for 24 h. The lack of infectious titer was confirmed with median tissue culture infectious dose ($TCID_{50}$) assays on VeroE6 cells.

The droplet with viable SARS-CoV-2 (50 μl) at a concentration of 1×10^7 PFU ml^{-1} in DMEM only medium was applied to a bare or coated surface. The DMEM medium consists of water and proteins, which is designed and manufactured to simulate the characteristic of body fluid [44,45]. Therefore, the DMEM medium can at least in part represent the body fluid generated during talking/coughing/sneezing. After 30 s waiting, surfaces were held aloft and 90 degree-tilted to allow free falling of the virus droplet. The droplet is pinned on a bare nonpermeable surface and wets the bare permeable surface, while it quickly rolls off the coated surfaces. Each surface was then submerged in 5 ml of phosphate-buffered saline (PBS) and was incubated for 10 min at room temperature. After incubation, 100 μl of the virus-containing PBS was aspirated and mixed with 400 μl of AVL buffer for further RNA extraction sampling following the QIAamp® Viral RNA Mini Handbook.

We perform RNA extraction instead of viability assays for two reasons. First, RNA extraction detects the amount of total viral genome while the viability assay (plaque assay) detects only the infectious virus particle. In this regard, the results from RNA extraction will provide a more complete picture of the virus adhesion test. Second, for many coated surfaces that we tested, only a trace amount of virus is retained on the substrates. In this scenario, RNA extraction, which has a better sensitivity than viability assays (plaque assays), will have a higher probability of detecting the signals.

Moreover, 9×10^7 virus gene copy is obtained when 50 μl of the virus at 1×10^7 PFU ml^{-1} is submerged in 5 ml of PBS, incubated for 10 min at room temperature, and 100 μl of the solution is subsequently extracted. As a control, 3.33%–100% recoveries are obtained from the bare surfaces, ranging from 3×10^6 (fabric) to 9×10^7 (mask) virus gene copy.

2.3. RNA extraction and quantitative real-time reverse transcription-polymerase chain reaction (qRT-PCR)

100 μl of the virus-containing PBS solution was lyzed with 400 μl of AVL buffer and was subsequently extracted for total RNA with a QIAamp viral RNA mini kit (Qiagen, Hilden, Germany). Quantitative real-time one-step qRT-PCR was used for quantitation of residual SARS-CoV-2 using a QuantiNova Probe RT-PCR kit (Qiagen) with a LightCycler 480

Real-Time PCR System (Roche, Basel, Switzerland) as we previously described [46]. The primers and probe sequences were previously reported [47] and were against the RNA-dependent RNA polymerase/helicase (RdRP/Hel) gene region of SARS-CoV-2: Forward primer: 5′-CGCATACAGTCTTRCAGGCT-3'; reverse primer: 5′-GTGTGATGTTGAWATGACATGGTC-3'; SARS-CoV-2 specific probe: 5′-FAM-TTAAGATGTGGTGCTTGCATACGTAGAC-IABkFQ-3'.

2.4. $TCID_{50}$ assay for antiviral effects of silver and copper nanoparticles

In order to test the antiviral effect of copper and silver nanoparticles, 500 μl of SARS-CoV-2 virus stock (1×10^7 PFU ml^{-1} in DMEM only medium) were mixed with 500 μl of 1000 ppm copper nanoparticles in H_2O, silver nanoparticles in H_2O, or H_2O. The mixtures were incubated for 24 h at 4 °C to allow full contact of viral particles and nanoparticles. At the same time, VeroE6 cells were seeded in 96 well plates at the concentration of 2×10^4 per well. After 24 h of incubation, the infectious titers of the virus-containing mixtures were quantified with $TCID_{50}$ assays. In brief, the virus-containing mixtures were serially diluted with DMEM only medium. The diluted mixtures were added to VeroE6 cells and infectious titers were quantified at 72 h after infection.

2.5. Sandpaper abrasion test

In the abrasion test, the super-repellent surfaces were placed face-down to the sandpaper (Standard glasspaper, 2000 cw) [48]. The surfaces were longitudinally abraded for 2 cm using the sandpaper under a pressure of ~0.2 kPa and then abraded backward for another 2 cm. This process is defined as one cycle. The virus adhesion test was conducted after abrasion for 50 cycles and 100 cycles. A solid with a mass of 8 g is placed on top of the samples (2cm × 2 cm) to maintain a constant pressure of ~0.2 kPa over the 50/100 abrasion cycles.

2.6. Virus residue detection using fluorescence imaging

The 10-μl probe liquid [fluorescein isothiocyanate (FITC)-BSA (5 mg ml^{-1}) in the inactivated SARS-CoV-2 virus solution] was released to allow rolling on the tested surface. The droplet traces were observed by fluorescence imaging using an inverted fluorescence microscope (Nikon Eclipse, TS100) equipped with a high-speed camera (Phantom, M110). The fluorescence of FITC-BSA was excited using a 490-nm light source.

2.7. Fabrication and characterization

To fabricate SHP SiO_2 coated surfaces, commercial spray, Glaco (Soft99), was used to render the substrate superhydrophobic by spray coating. The coated surface was then baked at 80 °C for 30 min to enhance the inter-particle binding.

To fabricate SAP SiO_2 coated surfaces, the suspension of polysiloxane/silica was prepared through hydrolytic condensation of 1*H*,1*H*,2*H*,2*H*-perfluorodecyltriethoxysilane and TEOS in the presence of silica nanoparticles. First, silica nanoparticles (0.1 g) were dispersed in a solution containing 44 ml of ethanol and 6 ml of ammonia aqueous solution. The mixture was ultrasonicated for 30 min. Then 1*H*,1*H*,2*H*,2*H*-perfluorodecyltriethoxysilane (150 μl) and TEOS (150 μl) were injected with vigorous stirring at 600 rpm. After reaction under room conditions for 24 h, a polysiloxane/silica suspension was formed. By spray coating the suspension (10 ml) onto a vertically placed substrate using an airbrush (Paasche H-SET) with 0.2 MPa nitrogen, a superamniphobic surface was prepared.

The SOP SiO_2 surface was prepared by modifying the previously reported superamphiphobic surface based on candle soot [31,49]. The glass slide (Luoyang Tengjing glass Co. Ltd) was first coated with candle soot and then placed in a desiccator together with 1 ml of tetraethoxysilane and 1 ml of ammonia hydroxide. The desiccator was closed, and the vacuum was maintained for 18 h. Then, the carbon soot core was removed by annealing at 550 °C for 3 h in an oven. The annealed sample was treated with air plasma for 5 min using a plasma cleaner (Harrick, PDC-002-HP) at a high power (45 W). The sample was deposited with PFDTS (100 μl) in a vacuum for 2 h to decrease its surface energy. The sample was then heated at 130 °C for 30 min to remove the unreacted PFDTS, followed by heat treatment at 310 °C for 15 min.

To prepare the SHP TiO_2 solution, 1.00 g of 1*H*,1*H*,2*H*,2*H*-perfluorooctyltriethoxysilane was placed in 99 g of absolute ethanol, and the solution was mechanically stirred for 2 h. To the resulting solution, 6 g of titanium oxide nanoparticles and 6 g of Degussa P25 titanium oxide were added to make a paint-like suspension. In the following experiments, we used simply a syringe needle to paint the substrate, and the paint was then dried in air for 20 min.

To fabricate SHP CuO coated surfaces, the copper sheet was ultrasonically cleaned in ethanol and deionized water for 10 min, respectively, followed by washing with dilute hydrochloric acid (1 M) for 10 s to remove the native oxide layer. Then the copper sheet was immersed in a freshly mixed aqueous solution of 2.5 mol l^{-1} sodium hydroxide and 0.1 mol l^{-1} potassium persulfate at room temperature for 60 min, followed by thorough rinsing with deionized water and drying in a nitrogen stream. As a result of chemical etching, CuO nanoflakes with an average diameter ~3.0 μm were produced. The sample was deposited with PFDTS (100 μl) in a vacuum for 20 min to decrease its surface energy, followed by heat treatment at 150 °C in the air for 2 h to render the surface superhydrophobic.

To fabricate SHP Ag coated surfaces, the polished copper sheet was first cleaned through successive ultrasonic rinses in ethanol, acetone, and isopropanol, and then under nitrogen flow. Silver nanostructures were deposited onto copper by immersing the copper sheet into an aqueous silver nitrate solution (0.01 mol l^{-1}) for 45 s. Then, the sheet was washed with deionized water and dried under a nitrogen flow. Then, a fluorinated self-assembly monolayer was deposited onto the surface by immersing the sheet into a 1*H*,1*H*,2*H*,2*H*-perfluorodecanethiol in dichloromethane solution (0.001 mol l^{-1}) for 15 min. The fabrication was completed by washing the surface with fresh dichloromethane and drying under ambient conditions for 5 min.

To fabricate a PDMS micropost surface, a negative mold consisting of the hole array (diameter ~80 μm, depth ~60 μm, and pitch ~230 μm) was first fabricated on a silicon wafer (<100> type) with a thickness of 420 ± 5 μm by standard photolithography. A PDMS precursor containing a 10 weight % (wt %) curing agent (Sylgard 184 silicone elastomer kit) was thoroughly stirred and vacuumed for 1 h to remove internal gas. The prepared PDMS was then cast on the negative mold and vacuumed for 1 h, followed by curing at 80 °C for 1 h. The PDMS micropost surface was obtained after peeling the PDMS out of the mold. The nanotextured PDMS micropost surface was prepared by spray coating the SAP SiO_2 solution onto the PDMS micropost surface.

The physical structures of the coatings were imaged using a Hitachi S4800 scanning electron microscope. Energy-dispersive X-ray scattering was used to obtain the elemental mapping of various elements in super-repellent coatings. The contact angles were measured using a goniometer (DataPhysics, OCA 25). Contact angle measurements were taken by depositing a small droplet of liquid (~5 μl) onto the surface using a 1-ml syringe (Hamilton) equipped with a dosing needle of 0.23 mm outer diameter. The roll-off angles were measured by tilting a stage until the droplet (~5 μl) started to roll off the surface. The adhesive forces on diverse surfaces were measured using a tensiometer (DataPhysics, DCAT 25) by compressing and then retracting a 10 μl droplet. For the measurement, the droplet is attached to a metal holder of 2.5 mm diameter and pressed onto the surface with a compression distance of 0.5 mm. Afterwards, the droplet is pulled off until it detaches from the surfaces. The force–displacement diagram is recorded and the adhesive force is then calculated using the maximum force. Averages from at least three independent measurements are used.

2.8. Experiment of performance on PPE and frequently touched objects

To fabricate SAP SiO_2 coated glove and mask, the suspension of polysiloxane/silica (20 ml) was sprayed onto a vertically placed substrate using an airbrush (Paasche H-SET) with 0.2 MPa nitrogen.

To fabricate SHP SiO_2 coated button, doorknob and clothing, 0.5 ml of commercial spray, Glaco Soft99, was sprayed onto the substrates. The coated surface was then baked at 80 °C for 30 min to enhance interparticle binding.

3. Results and discussion

3.1. Virus repellency

We use viable SARS-CoV-2 for the virus adhesion test (see Materials and methods section for details). As the tiny droplets and the resulting virus aerosol are highly risky to the operator even in Biosafety Level 3 facility, we deposit a 50 μl virus-laden droplet, containing 1×10^7 PFU ml^{-1} viable SARS-CoV-2, on bare and coated substrates to perform the virus adhesion test (Movie S1). After 30 s, the substrates are tilted to 90° to remove any unattached solution and the SARS-CoV-2 remnants on contact regions are probed using quantitative real-time polymerase chain reaction (qRT-PCR). Daily encountered materials, including glass, fabric (polyester), steel, copper, mask, nitrile glove, and paper, are chosen as substrates. Six types of repellent coatings, including superhydrophobic (SHP), superamphiphobic (SAP), and superomniphobic (SOP) types, are fabricated by functionalizing diverse nanostructures, including SiO_2 nanoparticles (SHP and SAP SiO_2), soot-templated fractal SiO_2 network (SOP SiO_2), TiO_2 nanoparticles (SHP TiO_2), CuO nanoflakes (SHP CuO), and Ag nanocrystals (SHP Ag) [48–52]. The substrate and coating are paired on the basis of their compatibility.

Supplementary video related to this article can be found at https://doi.org/10.1016/j.mtbio.2021.100145

Unlike the firmly pinned droplets on pristine glass (Fig. 1a), on the coated surface, the virus solution minimizes the contact by forming a spherical droplet and rolls off the repellent slope in a frictionless manner, leaving behind no observable liquid residues (Fig. 1b and Movie S2) [31]. As shown in Fig. 1c and d, we quantify the retention of SARS-CoV-2 N_i (virus gene copy) on different coating–substrate pairs and detect a substantial reduction as high as seven orders of magnitude compared with that of the bare substrate N_0, generating a repelling rate $(N_0–N_i)/N_0$ as high as 99.99999%, a value surpassing the filtration rate of the N95 mask (e.g. 95%) and inactivation rate of the chemical disinfectant (e.g. 99.9% in 1 h) [53]. For the evaluated materials, superior repelling performance is generally conserved except for nitrile glove overlaid with SHP SiO_2 and SHP TiO_2. Such a failure is potentially caused by the coating exfoliation, a consequence of the poor interfacial bonding between the rigid coating and elastic-plastic sheet (Fig. S1). The SARS-CoV-2 repellency has some levels of variation across different substrates, as observed with the performance of the SHP SiO_2 coating peaks for paper but degrades on other substrates, signaling a pairwise optimization between the coating and substrate properties such as textures and flexibility.

Supplementary video related to this article can be found at https://doi.org/10.1016/j.mtbio.2021.100145

3.2. Interfacial virus retention

As shown in Fig. 2a, the scanning electron microscopy (SEM) image delineates the nanoscale topography whose geometry and interfacial chemistry work in concert to reduce the liquid/solid adhesion and consequently the liquid retention (Fig. S2). As shown in Fig. 2b, the nanotextures effectively withstand the impact of a SARS-CoV-2 droplet (Weber number = 5.5), as observed that the droplet rebounds more than six times before its final rest, acting as a soft elastic object (Movie S3). For different coating–substrate pairs, the virus-bearing droplets all exhibit a large contact angle (>150°) and a low roll-off angle (<5°), minimizing the liquid/solid contact and maximizing the in-plane liquid mobility (Fig. 2c, Fig. S3 and Table S1).

Supplementary video related to this article can be found at https://doi.org/10.1016/j.mtbio.2021.100145

Similar contact angles for different coating–substrate pairs indicate that the virus remnant is relatively independent of the substrate static wettability. Using a microforce sensing probe, we measure the vertical liquid adhesive force $F_\perp$ between the SARS-CoV-2 solution and coating. Unlike the static wettability, the $F_\perp$ scatters for different pairs (Fig. 2c). On glasses coated with SAP SiO_2, $F_\perp$ is only 0.29 μN. However, the force peaks at 59.37 μN on nitrile glove coated with SHP SiO_2, a wide range spanning three orders of magnitude. By plotting data in the logarithmic axis (Fig. 2d), the fitting between N and $F_\perp$ unfolds an interesting exponential relationship as $N \propto 1.26^{F_\perp}$, implying a rapid growth rate of N as $F_\perp$ increases. Given the fact that the transmission of SARS-CoV-2 is highly efficient, it is key to reduce the interfacial adhesion toward SARS-CoV-2-laden droplets to minimize the infection risk.

3.3. Microscale liquid retention

Such interfacial adhesion originates in the capillary bridges formed atop the nanotextures [54,55]. To sidestep the structural irregularities, we assume that the coating caps an isotropic nanopost array on the substrate. Along the apparent contact line, nanocapillary bridges are formed (Fig. 3a). An individual peripheral nanocapillary bridge generates a vertical force of $\oint_s \gamma \sin\theta^n ds - \Delta P \times (\pi a^2/4)$, where γ is the liquid surface tension, θ^n is the local contact angle along the nanopost perimeter s, ΔP is the Laplace pressure that relates to droplet radius R as $2\gamma/R$, and a is the diameter of the nanopost (Fig. 3b) [28]. The contribution from Laplace pressure is usually an order of magnitude smaller than that from the surface tension and thus reduces the force into $\oint_s \gamma \sin\theta^n ds$. The local contact angle θ^n is smaller along the outer edge of the nanopost than that along the interior edge. As a SARS-CoV-2 droplet departs the surface, nanocapillary bridges stretch, gradually reducing the outermost θ^n. Once the local θ^n reaches the intrinsic receding contact angle, the contact line recedes atop the nanopost (Fig. 3c). Depending on the parameters such as droplet velocity and stretching angles, the capillary bridge eventually detaches the post through absolute receding or partial pinch-off, potentially leaving diminutive residues [56]. Such liquid remnants retain SARS-CoV-2 on the surfaces and are too diminutive to be quantified with available techniques, especially on the irregular nanostructures with super-repellency. We then fabricate a pristine and a nanotextured micropost array as modeled surfaces to study the correlation between $F_\perp$ and liquid residues (Fig. 3e and f).

The overall adhesion is collectively contributed by the dynamics of all capillary bridges along the apparent contact line. Paxson et al. proposed an effective pinned fraction φ, defined as the ratio of the length of the actual peripheral contact line to the apparent one as ns/l_{app}, where n is the number of peripheral capillary bridges and l_{app} is the apparent contact line length [57]. Such pinning is self-similar at the microscale and nanoscale. On an isotropic nanopost array, the pinned fraction φ is determined by the pitch τ as s/τ. By simply assuming that the localized contact angle atop the nanopost is the intrinsic receding contact angle θ_{rec}, the vertical adhesive force can be simplified as $F_\perp = \varphi l_{app}\gamma \sin\theta_{rec}$. For sparsely distributed sharp nanostructures, the pinned fraction φ^n can be as low as ~0.1. Thus, the pinned fraction φ^m values are much higher on pristine microposts than those of the nanotextured microposts ($\varphi^m \varphi^n$). As shown in Fig. 3d, the $F_\perp$ of SARS-CoV-2 droplets on pristine microposts surpass the nanotextured microposts by 89.66 μN (see also Fig. S4 and Movie S4). The side view in Fig. 3g shows that the θ_{rec} on the pristine micropost is so small that the value cannot be obtained by stretching the capillary bridge. As a result, the liquid bridge undergoes pinch-off and leaves substantial SARS-CoV-2 liquid residue atop the pristine micropost

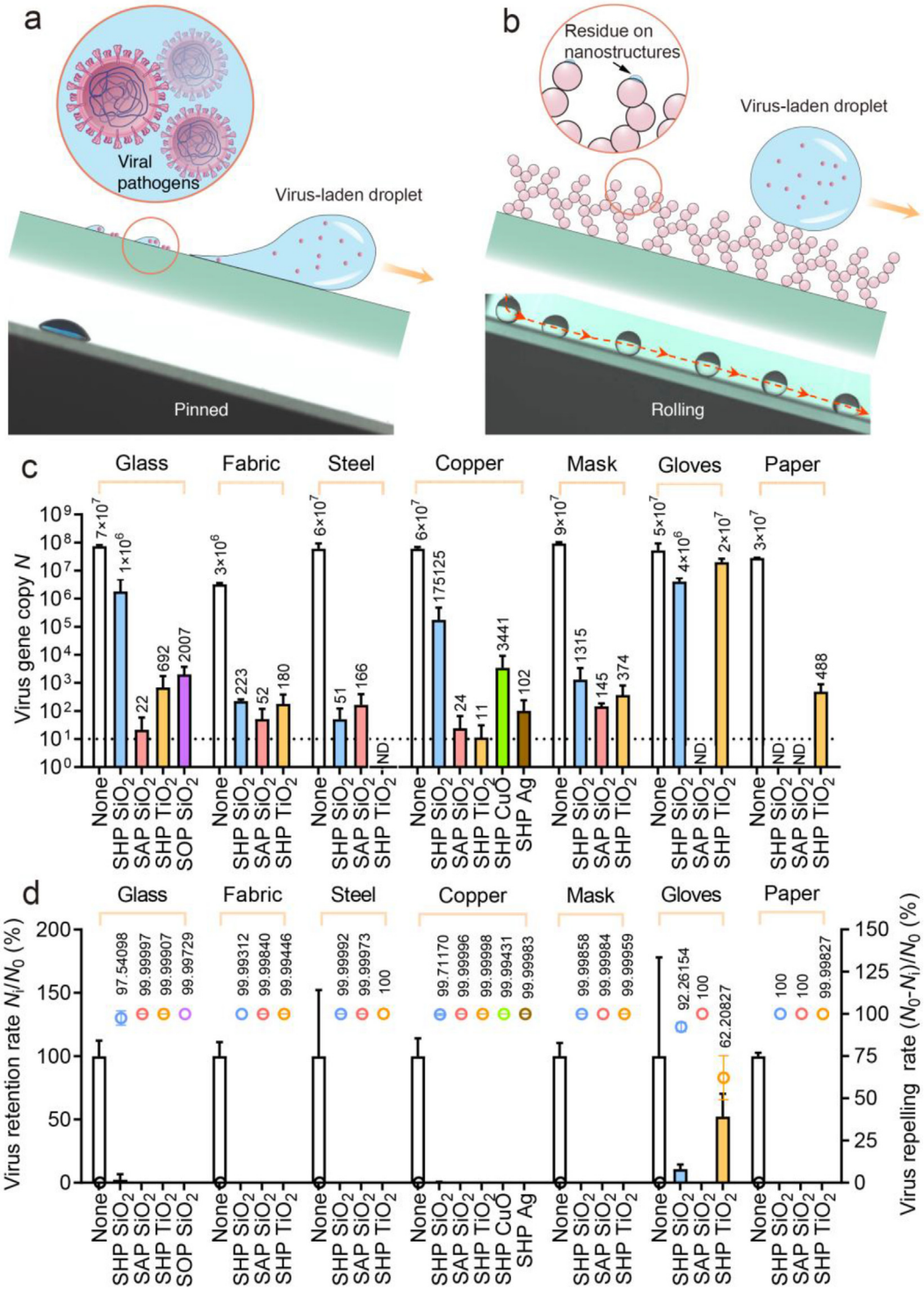

Fig. 1. SARS-CoV-2 repellency. Schematics and chronophotographs of SARS-CoV-2-laden droplets slide/roll on (a) bare glass and (b) liquid-repellent surface. (c) SARS-CoV-2 gene copy *N* determined through quantitative real-time polymerase chain reaction shows seven orders of magnitude reduction in SARS-CoV-2 retention using the liquid-repellent coating. ND represents "not detected" and is denoted by the dashed line. Error bar denotes standard deviation of three independent experiments. (d) SARS-CoV-2 retention rate N_i/N_0 (denoted by columns) and SARS-CoV-2 repelling rate $(N_0–N_i)/N_0$ (denoted by dots) calculated from (c).

(Movie S5). However, the nanoscale coating significantly increases the microscale θ_{rec} to be nearly 150°, so that the contact line can readily recede on nanotextured micropost without obvious pinning (Fig. 3h). Further fluorescence imaging in Fig. 3i and j contrasts the expected dyed SARS-CoV-2 solution residues where the residue is observed atop the pristine micropost and cannot be identified in the nanotextured one. The fluorescence intensity and fraction area on nanotextured microposts are only 3.6% and 1.1% of those on the pristine microposts (Fig. S5). Thus, to prohibit the liquid retention and subsequently the SARS-CoV-2 remnants, we must decrease φ by designing the hierarchical roughness and increase

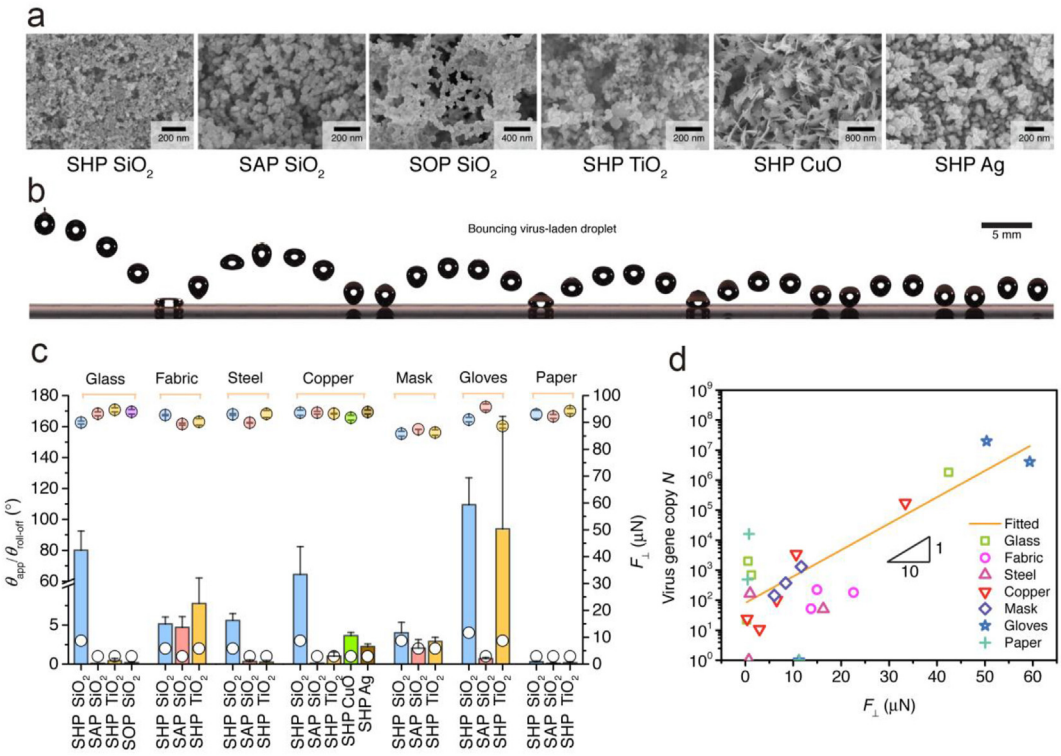

Fig. 2. Interfacial virus retention. (a) SEM images showing the coatings consisting of SiO_2 nanoparticles (SHP and SAP SiO_2), soot-templated fractal SiO_2 network (SOP SiO_2), TiO_2 nanoparticles (SHP TiO_2), CuO nanoflakes (SHP CuO), and Ag nanocrystals (SHP Ag). (b) Chronophotographs showing six rebounds of a 5 μl SARS-CoV-2-laden droplet liberating from a height of ~9 mm on the underlying SOP SiO_2 surface. (c) SARS-CoV-2-laden droplets have a large contact angle θ_{app} (>150°) and a low roll-off angle $\theta_{roll\text{-}off}$ (<5°) for different coating–substrate pairs, but the adhesions $F_\perp$ scatters much. Solid and open circles, respectively, denote θ_{app} and $\theta_{roll\text{-}off}$. Columns denote the vertical liquid/solid adhesion $F_\perp$. Error bar denotes standard deviation of three independent experiments. (d) The SARS-CoV-2 remnant N grows exponentially as $F_\perp$ increases.

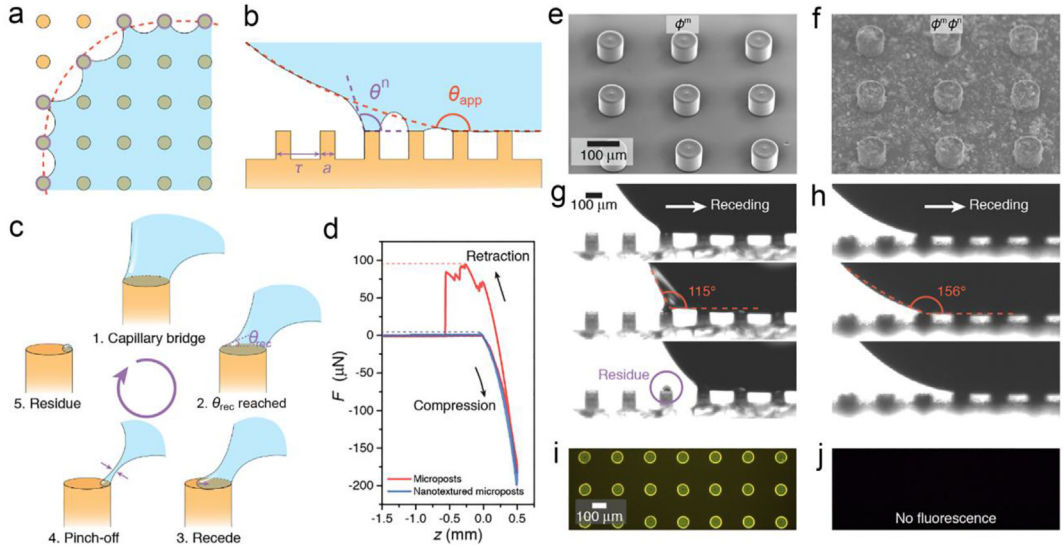

Fig. 3. Microscale liquid retention. (a) Collective pinning of the peripheral local capillary bridges. Red dashed line and purple circles denote apparent and actual contact lines, respectively. (b) Local capillary bridges on microstructured surfaces. Red and purple dashed lines denote the macroscopic and microscopic contact angles, respectively. (c) Atop micropost, the capillary bridge recedes as the receding contact angle θ_{rec} is reached, otherwise, the capillary bridge is pinned and further stretching pinches the bridge, leaving tiny amount of liquid residue. (d) Force–displacement curves contrast the maximum $F_\perp$ on surfaces capped with pristine and nanotextured microposts. SEM images showing textures of (e) pristine and (f) nanotextured micropost array. Sequential images showing the microcapillary bridges' receding behaviors on the (g) pristine and (h) nanotextured micropost. (i) Fluorescence signals of SARS-CoV-2 liquid retention atop pristine microposts. (j) No SARS-CoV-2 liquid residues can be observed on the nanotextured microposts. Panels a and b are reprinted with permission from Ref. [28], Copyright 2020, Elsevier.

θ_{rec} by decreasing the surface energy, two critical parameters depicting the interfacial adhesion. As the concentration of virus and protein within the droplet will have an effect on the surface tension of the liquid and thus the interfacial adhesion, future works are needed to examine their effects on virus residue.

Supplementary video related to this article can be found at https://doi.org/10.1016/j.mtbio.2021.100145

3.4. Sneeze repellency

We then test the utility by simulating an interaction between a sneeze and the repellent coating (Movie S6). As shown in Fig. 4a, inactivated-SARS-CoV-2-laden droplets of sizes ranging from ~10 to ~2000 μm are sprayed toward a glass slide coated with the SHP TiO_2 coating through an airbrush. A large SARS-CoV-2 droplet with a diameter of 1021 μm impinges the surface at 4.8 ms and immediately rebounds at 10.6 ms. At the end of the violent spraying (105.2 ms), a diminutive SARS-CoV-2 droplet with a diameter of ~18 μm can still be effectively shed off, maintaining the hygiene and cleanness of the surface (Fig. 4b). For mostly mild-to-moderate cases [58], the virus fraction is less than 0.01% for droplets below 18 μm. Therefore, more than 99.99% of the droplets with a diameter less than 18 μm will not carry any virus [59]. Thus, the SHP TiO_2 coating is effective for sneeze shielding as droplets of diameter being above 18 μm can be quickly shed off. After sneeze impact, the fluorescence intensity and fraction area on TiO_2 coated glass are only 0.5% and 0.6% of those on the pristine glass (Fig. 4c and d), confirming the function of the coating.

Supplementary video related to this article can be found at https://doi.org/10.1016/j.mtbio.2021.100145

3.5. Composite antipathogen coatings

Antimicrobial ingredients can also be incorporated into the super-liquid-repellent coatings to form composite antipathogen coatings that both repel the pathogens and inactivate the trace amount of residual pathogens left on the coating. Silver nanoparticles (nano-Ag) and copper nanoparticles (nano-Cu) have been exploited as antimicrobial agents [26]. However, their effects against SARS-CoV-2 are mostly unknown. We then first examine the antiviral efficiency of nano Ag (~15 nm) and nano Cu (~60 nm) toward SARS-CoV-2 (see the Experimental section for details). As shown in Fig. 5a, both nano-Ag and nano-Cu demonstrate a remarkable anti-SARS-CoV-2 effect as evidenced by the significantly reduced infectious SARS-CoV-2 virus particles, which is determined by $TCID_{50}$ assays. Specifically, nano-Cu demonstrated a 10-fold decrease in infectious SARS-CoV-2 titer and nano-Ag demonstrated a 426-fold decrease in infectious SARS-CoV-2 titer.

Because of the outstanding anti-SARS-CoV-2 property of nano-Ag and super-repellency of SAP SiO_2 coating, we then evaluate the virus-repellent effect of nano-Ag-doped SAP SiO_2 coating (SAP SiO_2+1% nano Ag) by performing a virus adhesion test. As shown in Fig. 5b, the size of nano-Ag ranges from ~3 nm to ~42 nm. Adding 1%wt nano Ag into the SAP SiO_2 coating has no effect on the morphology of coating (Fig. 5c) and the nano-Ag is homogeneously distributed in the composite coating (Fig. 5d). As shown in Fig. 5e and f, the 1% nano Ag-doped SiO_2 coating largely retains its SARS-CoV-2 repellent capacity on diverse substrates except for nitrile glove. Such failure may be caused by the coating exfoliation as the hydrophilic nano-Ag may weaken the interfacial bonding between SAP SiO_2 coating and elastic-plastic sheet. Though future work is still required to examine the SARS-CoV-2 activity on the composite antiviral coating, our results demonstrate that nano-Ag is an effective antiviral agent against SARS-CoV-2 and it is feasible to introduce antiviral additives like nano-Ag into the super-liquid-repellent coating to form a composite antiviral coating that both repels pathogens and inactivates the residual pathogens.

3.6. Durability and versatility

The mechanical durability of the coatings is tested by performing a virus adhesion test after sandpaper abrasion. The result shows that the microtextures of the coatings are largely retained after the sandpaper abrasion (Fig. S6), being in agreement with the result reported in the literature [48], and thus maintain their super-repellency to droplets loaded with SARS-CoV-2 (Fig. S7). We then perform the virus adhesion test after different abrasion cycles and find that the virus-repellent performance of the coatings can essentially maintain up to 100 abrasion cycles (Fig. 6a). It becomes counter-intuitive as some coatings such as

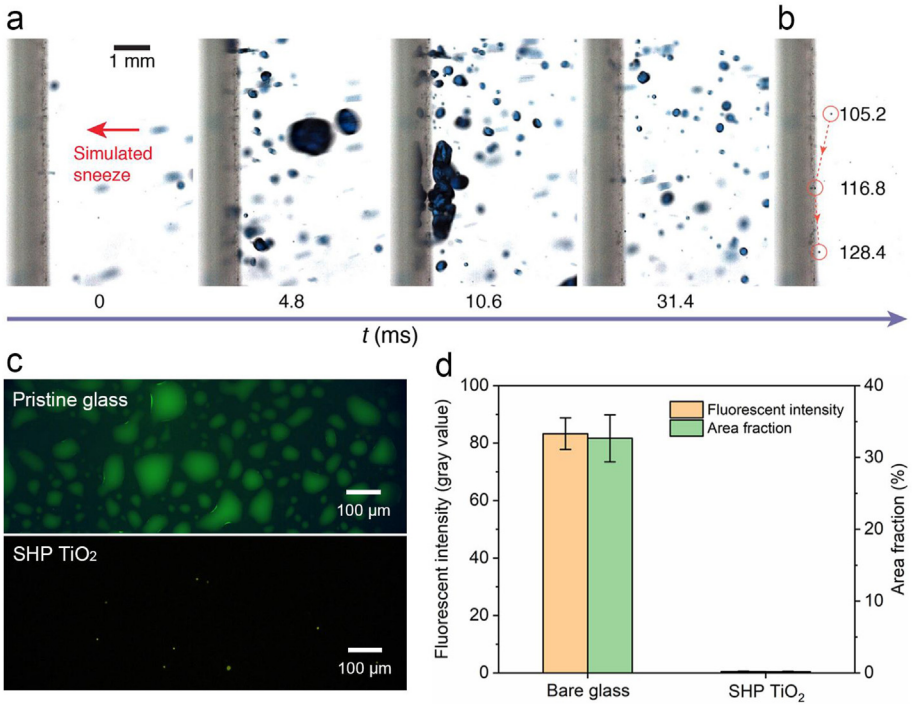

Fig. 4. Sneeze repellency. (a) Sequential images showing high-momentum SARS-CoV-2 droplets of simulated sneeze rebound off the SHP TiO_2 coated glass. (b) Chronophotographs showing the shedding of a ~18 μm SARS-CoV-2 droplet off the surface. (c) Fluorescence imaging contrasting the virus-laden droplet residue on pristine glass and SHP TiO_2 coated glass after sneeze impact. The virus-laden droplet is labeled with fluorescein isothiocyanate (FITC)-BSA (5 mg ml^{-1}). (d) Fluorescence intensity and area fraction of the images in (c), showing the remarkably reduced SARS-CoV-2 liquid residue on the coated surface. Error bars denote standard deviation over three independent experiments.

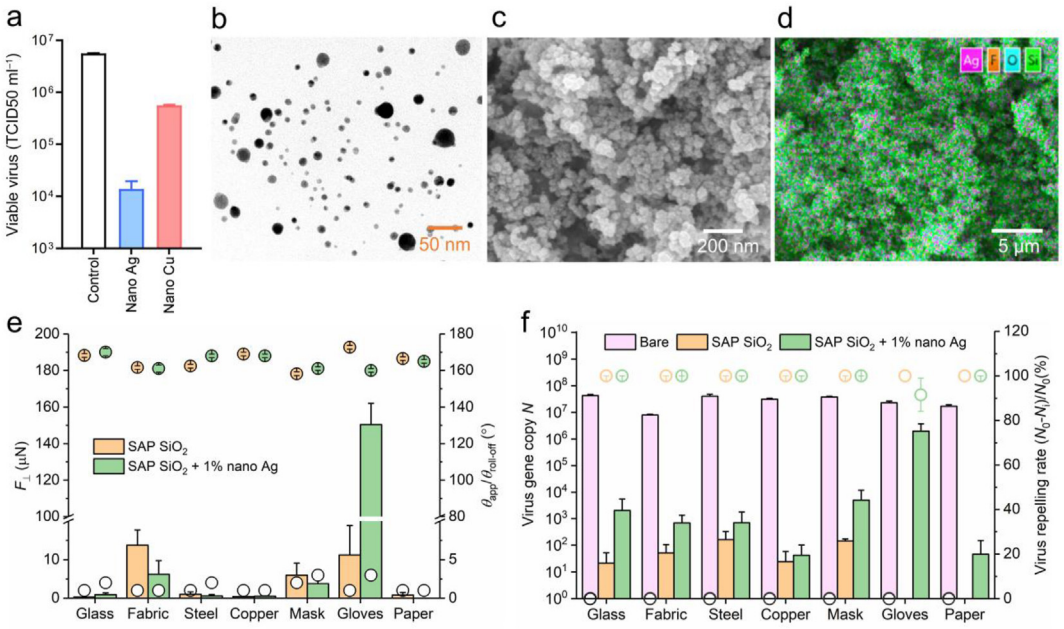

Fig. 5. Composite antiviral coating. (a) Antiviral effects of silver nanoparticles (nano-Ag) and copper nanoparticles (nano-Cu) toward SARS-CoV-2. (b) Transmission electron microscopy (TEM) image showing nano-Ag with a diameter of ~3 nm–~42 nm. (c) SEM images showing the nanostructures of nano-Ag-doped SAP SiO_2 coating. (d) Energy-dispersive X-ray spectroscopy (EDX) mapping showing that the silver nanoparticles are evenly distributed in the SAP SiO_2 coating. (e) The adhesive force $F_\perp$, static contact angle θ_{app}, and roll-off angle $\theta_{roll\text{-}off}$ of virus-laden droplet on the SAP SiO_2 coating doped with 1%wt nano Ag. Columns denote the vertical liquid/solid adhesion $F_\perp$. Solid and open circles, respectively, denote θ_{app} and $\theta_{roll\text{-}off}$. Error bar denotes standard deviation of three independent experiments. (f) The super-repellency of the coating to SARS-CoV-2 is largely maintained regardless of the participation of nano-Ag. Columns denote the SARS-CoV-2 gene copy N and open circles denote the SARS-CoV-2 repelling rate $(N_0–N_i)/N_0$. Error bar denotes standard deviation of three independent experiments.

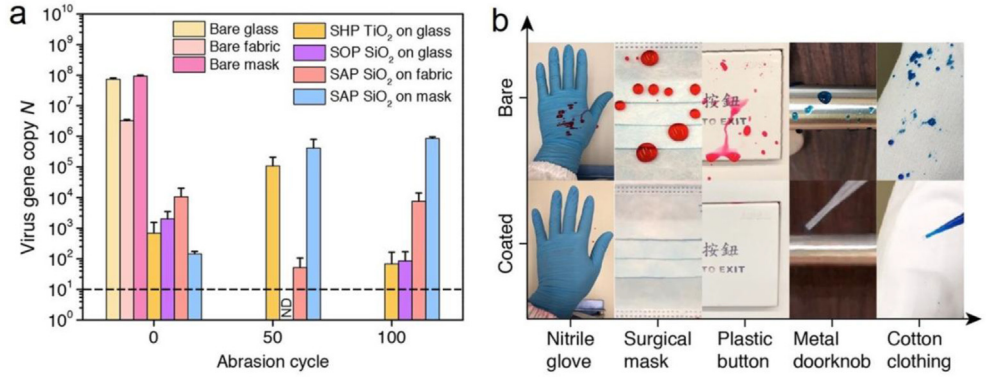

Fig. 6. Durability and versatility. (a) Virus repellency of the super-repellent coatings on glass, fabric, and mask after abrasion. ND represents "not detected" and is denoted by the dashed line. Error bars denote standard deviation of three independent experiments. (b) Photos contrasting the retention of SARS-CoV-2-loaded droplets on various substrates: glove and mask coated with the SAP SiO_2; button, doorknob, and clothing coated with the SHP SiO_2.

SAP SiO_2 on fabric become more virally repellent after abrasion. Such effect is potentially caused by additional microscale roughness introduced by the abrasion which further improves the liquid repellency (Fig. S6).

In real-life situations, once the pathogen-laden droplets move off the coated frequently touched surfaces, they subsequently deposit on the ground or other nonfrequently touched surfaces, where the infection risk is greatly reduced. Moreover, disinfection is only required for the ground and noncoated surfaces rather than all surfaces, thus reducing the usage of disinfectants and lowering their harm to the human body [60]. We then treat personal protection equipment (PPE) and frequently touched objects such as gloves, masks, buttons, doorknobs, and clothing with the repellent coating (Fig. 6b and Movie S7). Coated objects exhibit excellent repellency to inactivated SARS-CoV-2 droplets which confirms that the coating can adapt to various substrates with contrasting composition, texture, and geometry, showing its potential for wide applications. Aside from the high performances of these coatings, the large-area and low-cost fabrication [50,61], increased mechanical robustness [49,62], and long-term stability [63] will pave the way for their practical applications for infection control.

Supplementary video related to this article can be found at https://doi.org/10.1016/j.mtbio.2021.100145

4. Conclusions

Infection prevention and control of pandemic are critical to human beings, considering the fact that our society is constantly battered by widespread infectious diseases, for example, the outbreak of severe acute respiratory syndrome (SARS) in 2003, the Middle East respiratory syndrome in 2012, and now the COVID-19. Here, we demonstrate that using

a super-liquid-repellent coating, SARS-CoV-2-laden droplets can be effectively repelled, an effective and efficient way to block the two aforementioned routes of SARS-CoV-2 transmission. The SARS-CoV-2 remnants scale exponentially with the liquid/solid adhesion, showing the key role played by the liquid/solid adhesion in reducing the pathogen remnants. Antipathogen ingredients like silver nanoparticles can also be incorporated into the coating to form a composite antipathogen coating that not only repels but also inactivates pathogens. Overall, the innovative pathogen prevention strategy demonstrated in this study can be widely applied and can thus play an essential role in the control and prevention of infectious organisms both in everyday life and during pandemics.

Author contributions

L.W. and H.C. supervised the study. L.W., H.C., and X.T. conceived the project. L.W., H.C., W.L., and Y.W. designed the project. W.L., Y.W., and T.T.T.Y. performed the experiments. X. H. contributed to the characterization of super-repellent surfaces. J. L. contributed to the fabrication of the PDMS micropost arrays surface. N. H. contributed to fluorescence imaging. L.W., H.C., W.L., X.T., and J.F.W.C. analyzed the data. J.F.W.C. provided key reagents. L.W., H.C., X.T., and W.L. wrote the manuscript with comments from all authors.

Data and materials availability

All data are provided in the article or the supplementary file.

Declaration of competing interest

The authors declare that they have no known competing financial interests or personal relationships that could have appeared to influence the work reported in this paper.

Acknowledgments

The authors wish to thank Prof. B.P. Chan for equipment support. The financial support from the Research Grants Council of Hong Kong (GRF 17205421, 17204420, 17123920, 17210319, 17204718, 17237316, CRF C1018-17G, and TRS T11/707/15) and the University of Hong Kong (URC 201511159108) is gratefully acknowledged. This work was also supported in part by the Zhejiang Provincial, Hangzhou Municipal, and Lin'an County Governments.

Appendix A. Supplementary data

Supplementary data to this article can be found online at https://doi.org/10.1016/j.mtbio.2021.100145.

References

[1] D. Kim, S. Kim, J. Park, H.R. Chang, J. Chang, J. Ahn, H. Park, J. Park, N. Son, G. Kang, A high-resolution temporal atlas of the SARS-CoV-2 translatome and transcriptome, Nat. Commun. 12 (2021), 5120.
[2] WHO Solidarity Trial Consortium, Repurposed antiviral drugs for COVID-19—interim WHO SOLIDARITY trial results, N. Engl. J. Med. 384 (2021) 497–511.
[3] M. Hoffmann, P. Arora, R. Groß, A. Seidel, B.F. Hörnich, A.S. Hahn, N. Krüger, L. Graichen, H. Hofmann-Winkler, A. Kempf, SARS-CoV-2 variants B. 1.351 and P. 1 escape from neutralizing antibodies, Cell 184 (2021) 2384–2393.
[4] Q. Li, J. Nie, J. Wu, L. Zhang, R. Ding, H. Wang, Y. Zhang, T. Li, S. Liu, M. Zhang, C. Zhao, H. Liu, L. Nie, H. Qin, M. Wang, Q. Lu, X. Li, J. Liu, H. Liang, Y. Shi, Y. Shen, L. Xie, L. Zhang, X. Qu, W. Xu, W. Huang, Y. Wang, SARS-CoV-2 501Y.V2 variants lack higher infectivity but do have immune escape, Cell 184 (2021) 2362–2371.
[5] D. Zhou, W. Dejnirattisai, P. Supasa, et al., Evidence of escape of SARS-CoV-2 variant B.1.351 from natural and vaccine-induced sera, Cell 184 (2021) 2348–2361.
[6] W.J. Wiersinga, A. Rhodes, A.C. Cheng, S.J. Peacock, H.C. Prescott, Pathophysiology, transmission, diagnosis, and treatment of coronavirus disease 2019 (COVID-19): a review, JAMA 324 (2020) 782–793.
[7] K. Ng, B.H. Poon, T.H. Kiat Puar, J.L. Shan Quah, W.J. Loh, Y.J. Wong, T.Y. Tan, J. Raghuram, COVID-19 and the risk to health care workers: a case report, Ann. Intern. Med. 172 (2020) 766–767.
[8] P.Y. Chia, K.K. Coleman, Y.K. Tan, et al., Detection of air and surface contamination by SARS-CoV-2 in hospital rooms of infected patients, Nat. Commun. 11 (2020), 2800.
[9] X. Xue, J.K. Ball, C. Alexander, M.R. Alexander, All surfaces are not equal in contact transmission of SARS-CoV-2, Matter 3 (2020) 1433–1441.
[10] S.W.X. Ong, Y.K. Tan, P.Y. Chia, T.H. Lee, O.T. Ng, M.S.Y. Wong, K. Marimuthu, Air, surface environmental, and personal protective equipment contamination by severe acute respiratory syndrome coronavirus 2 (SARS-CoV-2) from a symptomatic patient, JAMA 323 (2020) 1610–1612.
[11] J. Otter, C. Donskey, S. Yezli, S. Douthwaite, S. Goldenberg, D. Weber, Transmission of SARS and MERS coronaviruses and influenza virus in healthcare settings: the possible role of dry surface contamination, J. Hosp. Infect. 92 (2016) 235–250.
[12] S.E. Crawford, S. Ramani, J.E. Tate, U.D. Parashar, L. Svensson, M. Hagbom, M.A. Franco, H.B. Greenberg, M. O'Ryan, G. Kang, Rotavirus infection, Nat. Rev. Dis. Prim. 3 (2017), 17083.
[13] G.U. Lopez, C.P. Gerba, A.H. Tamimi, M. Kitajima, S.L. Maxwell, J.B. Rose, Transfer efficiency of bacteria and viruses from porous and nonporous fomites to fingers under different relative humidity conditions, Appl. Environ. Microbiol. 79 (2013) 5728–5734.
[14] A. Kramer, I. Schwebke, G. Kampf, How long do nosocomial pathogens persist on inanimate surfaces? A systematic review, BMC Infect. Dis. 6 (2006), 130.
[15] N. Van Doremalen, T. Bushmaker, D.H. Morris, M.G. Holbrook, A. Gamble, B.N. Williamson, A. Tamin, J.L. Harcourt, N.J. Thornburg, S.I. Gerber, Aerosol and surface stability of SARS-CoV-2 as compared with SARS-CoV-1, N. Engl. J. Med. 382 (2020) 1564–1567.
[16] A.W.H. Chin, J.T.S. Chu, M.R.A. Perera, K.P.Y. Hui, H.-L. Yen, M.C.W. Chan, M. Peiris, L.L.M. Poon, Stability of SARS-CoV-2 in different environmental conditions, Lancet Microbe 1 (2020) e10.
[17] P. Liu, M. Yang, X. Zhao, Y. Guo, L. Wang, J. Zhang, W. Lei, W. Han, F. Jiang, W.J. Liu, Cold-chain transportation in the frozen food industry may have caused a recurrence of COVID-19 cases in destination: successful isolation of SARS-CoV-2 virus from the imported frozen cod package surface, Biosaf. Health 2 (2020) 199–201.
[18] H. Kanamori, D.J. Weber, W.A. Rutala, The role of the healthcare surface environment in SARS-CoV-2 transmission and potential control measures, Clin. Infect. Dis. (2020) ciaa1467.
[19] W. Ahmed, Z. Zhai, C. Gao, Adaptive antibacterial biomaterial surfaces and their applications, Mater. Today Bio 2 (2019) 100017.
[20] Y. Qian, K. Willeke, S.A. Grinshpun, J. Donnelly, C.C. Coffey, Performance of N95 respirators: filtration efficiency for airborne microbial and inert particles, Am. Ind. Hyg. Assoc. J. 59 (1998) 128–132.
[21] L. Bourouiba, Turbulent gas clouds and respiratory pathogen emissions: potential implications for reducing transmission of COVID-19, JAMA 323 (2020) 1837–1838.
[22] L. Bourouiba, E. Dehandschoewercker, J.W. Bush, Violent expiratory events: on coughing and sneezing, J. Fluid Mech. 745 (2014) 537–563.
[23] H. Huang, C. Fan, M. Li, H.-L. Nie, F.-B. Wang, H. Wang, R. Wang, J. Xia, X. Zheng, X. Zuo, COVID-19: a call for physical scientists and engineers, ACS Nano 14 (2020) 3747–3754.
[24] L.H. Nguyen, D.A. Drew, M.S. Graham, et al., Risk of COVID-19 among front-line health-care workers and the general community: a prospective cohort study, Lancet Public Health 5 (2020) e475–e483.
[25] E. O'Kelly, A. Arora, S. Pirog, J. Ward, P.J. Clarkson, Comparing the fit of N95, KN95, surgical, and cloth face masks and assessing the accuracy of fit checking, PLoS One 16 (2021), e0245688.
[26] S.M. Imani, L. Ladouceur, T. Marshall, R. Maclachlan, L. Soleymani, T.F. Didar, Antimicrobial nanomaterials and coatings: current mechanisms and future perspectives to control the spread of viruses including SARS-CoV-2, ACS Nano 14 (2020) 12341–12369.
[27] M. Ma, R.M. Hill, Superhydrophobic surfaces, Curr. Opin. Colloid Interface Sci. 11 (2006) 193–202.
[28] X. Tang, Y. Tian, X. Tian, W. Li, X. Han, T. Kong, L. Wang, Design of multi-scale textured surfaces for unconventional liquid harnessing, Mater. Today 43 (2020) 62–83.
[29] X. Tang, P. Zhu, Y. Tian, X. Zhou, T. Kong, L. Wang, Mechano-regulated surface for manipulating liquid droplets, Nat. Commun. 8 (2017) 14831.
[30] A.K. Epstein, T.-S. Wong, R.A. Belisle, E.M. Boggs, J. Aizenberg, Liquid-infused structured surfaces with exceptional anti-biofouling performance, Proc. Natl. Acad. Sci. U.S.A. 109 (2012) 13182–13187.
[31] W. Li, X. Tang, L. Wang, Photopyroelectric microfluidics, Sci. Adv. 6 (2020), eabc1693.
[32] Y. Koc, A.J. de Mello, G. McHale, M.I. Newton, P. Roach, N.J. Shirtcliffe, Nano-scale superhydrophobicity: suppression of protein adsorption and promotion of flow-induced detachment, Lab Chip 8 (2008) 582–586.
[33] V. Jokinen, E. Kankuri, S. Hoshian, S. Franssila, R.H. Ras, Superhydrophobic blood-repellent surfaces, Adv. Mater. 30 (2018) 1705104.
[34] A. Tuteja, W. Choi, M. Ma, J.M. Mabry, S.A. Mazzella, G.C. Rutledge, G.H. McKinley, R.E. Cohen, Designing superoleophobic surfaces, Science 318 (2007) 1618–1622.
[35] H. Bellanger, T. Darmanin, E. Taffin de Givenchy, F. Guittard, Chemical and physical pathways for the preparation of superoleophobic surfaces and related wetting theories, Chem. Rev. 114 (2014) 2694–2716.
[36] Z. Chu, S. Seeger, Superamphiphobic surfaces, Chem. Soc. Rev. 43 (2014) 2784–2798.

[37] H.-J. Butt, C. Semprebon, P. Papadopoulos, D. Vollmer, M. Brinkmann, M. Ciccotti, Design principles for superamphiphobic surfaces, Soft Matter 9 (2013) 418–428.
[38] T.L. Liu, C.-J.C. Kim, Turning a surface superrepellent even to completely wetting liquids, Science 346 (2014) 1096–1100.
[39] A.K. Kota, G. Kwon, A. Tuteja, The design and applications of superomniphobic surfaces, NPG Asia Mater. 6 (2014), e109.
[40] X. Zhang, L. Wang, E. Levänen, Superhydrophobic surfaces for the reduction of bacterial adhesion, RSC Adv. 3 (2013) 12003–12020.
[41] P. Zhu, Y. Wang, H. Chu, L. Wang, Superhydrophobicity preventing surface contamination as a novel strategy against COVID-19, J. Colloid Interface Sci. 600 (2021) 613–619.
[42] H. Chu, J.F. Chan, T.T. Yuen, H. Shuai, S. Yuan, Y. Wang, B. Hu, C.C. Yip, J.O. Tsang, X. Huang, Y. Chai, D. Yang, Y. Hou, K.K. Chik, X. Zhang, A.Y. Fung, H.W. Tsoi, J.P. Cai, W.M. Chan, J.D. Ip, A.W. Chu, J. Zhou, D.C. Lung, K.H. Kok, K.K. To, O.T. Tsang, K.H. Chan, K.Y. Yuen, Comparative tropism, replication kinetics, and cell damage profiling of SARS-CoV-2 and SARS-CoV with implications for clinical manifestations, transmissibility, and laboratory studies of COVID-19: an observational study, Lancet Microbe 1 (2020) e14–e23.
[43] H. Chu, J.F.-W. Chan, Y. Wang, T.T.-T. Yuen, Y. Chai, H. Shuai, D. Yang, B. Hu, X. Huang, X. Zhang, SARS-CoV-2 induces a more robust innate immune response and replicates less efficiently than SARS-CoV in the human intestines: an ex vivo study with implications on pathogenesis of COVID-19, Cell. Mol. Gastroenterol. Hepatol. 11 (2020) 771–781.
[44] Ö. Bayrak, H. Ghahramanzadeh Asl, A. Ak, Comparison of SBF and DMEM in terms of electrochemical properties of common metallic biomaterials, Mater. Corros. 71 (2020) 209–221.
[45] J.T. Lee, Y. Leng, K.L. Chow, F. Ren, X. Ge, K. Wang, X. Lu, Cell culture medium as an alternative to conventional simulated body fluid, Acta Biomater. 7 (2011) 2615–2622.
[46] H. Chu, J.F. Chan, Y. Wang, T.T. Yuen, Y. Chai, Y. Hou, H. Shuai, D. Yang, B. Hu, X. Huang, X. Zhang, J.P. Cai, J. Zhou, S. Yuan, K.H. Kok, K.K. To, I.H. Chan, A.J. Zhang, K.Y. Sit, W.K. Au, K.Y. Yuen, Comparative replication and immune activation profiles of SARS-CoV-2 and SARS-CoV in human lungs: an ex vivo study with implications for the pathogenesis of COVID-19, Clin. Infect. Dis. 71 (2020) 1400–1409.
[47] H. Chu, B. Hu, X. Huang, Y. Chai, D. Zhou, Y. Wang, H. Shuai, D. Yang, Y. Hou, X. Zhang, T.T. Yuen, J.P. Cai, A.J. Zhang, J. Zhou, S. Yuan, K.K. To, I.H. Chan, K.Y. Sit, D.C. Foo, I.Y. Wong, A.T. Ng, T.T. Cheung, S.Y. Law, W.K. Au, M.A. Brindley, Z. Chen, K.H. Kok, J.F. Chan, K.Y. Yuen, Host and viral determinants for efficient SARS-CoV-2 infection of the human lung, Nat. Commun. 12 (2021) 134.
[48] Y. Lu, S. Sathasivam, J. Song, C.R. Crick, C.J. Carmalt, I.P. Parkin, Robust self-cleaning surfaces that function when exposed to either air or oil, Science 347 (2015) 1132–1135.
[49] X. Deng, L. Mammen, H.-J. Butt, D. Vollmer, Candle soot as a template for a transparent robust superamphiphobic coating, Science 335 (2012) 67–70.
[50] S. Dong, Y. Li, N. Tian, B. Li, Y. Yang, L. Li, J. Zhang, Scalable preparation of superamphiphobic coatings with ultralow sliding angles and high liquid impact resistance, ACS Appl. Mater. Interfaces 10 (2018) 41878–41882.
[51] Y. Liu, L. Moevius, X. Xu, T. Qian, J.M. Yeomans, Z. Wang, Pancake bouncing on superhydrophobic surfaces, Nat. Phys. 10 (2014) 515–519.
[52] X. Tang, L. Wang, Loss-free photo-manipulation of droplets by pyroelectro-trapping on superhydrophobic surfaces, ACS Nano 12 (2018) 8994–9004.
[53] S. Behzadinasab, A. Chin, M. Hosseini, L. Poon, W.A. Ducker, A surface coating that rapidly inactivates SARS-CoV-2, ACS Appl. Mater. Interfaces 12 (2020) 34723–34727.
[54] B.D. Hatton, J. Aizenberg, Writing on superhydrophobic nanopost arrays: topographic design for bottom-up assembly, Nano Lett. 12 (2012) 4551–4557.
[55] T.-S. Wong, A.P.-H. Huang, C.-M. Ho, Wetting behaviors of individual nanostructures, Langmuir 25 (2009) 6599–6603.
[56] S. Huang, J. Li, L. Liu, L. Zhou, X. Tian, Lossless fast drop self-transport on anisotropic omniphobic surfaces: origin and elimination of microscopic liquid residue, Adv. Mater. 31 (2019) 1901417.
[57] A.T. Paxson, K.K. Varanasi, Self-similarity of contact line depinning from textured surfaces, Nat. Commun. 4 (2013) 1492.
[58] Y. Pan, D. Zhang, P. Yang, L.L. Poon, Q. Wang, Viral load of SARS-CoV-2 in clinical samples, Lancet Infect. Dis. 20 (2020) 411–412.
[59] S. Anand, Y. Mayya, Size distribution of virus laden droplets from expiratory ejecta of infected subjects, Sci. Rep. 10 (2020), 21174.
[60] S. Subpiramaniyam, Outdoor disinfectant sprays for the prevention of COVID-19: are they safe for the environment? Sci. Total Environ. 759 (2020) 144289.
[61] L. Zhang, A.G. Zhou, B.R. Sun, K.S. Chen, H.-Z. Yu, Functional and versatile superhydrophobic coatings via stoichiometric silanization, Nat. Commun. 12 (2021), 982.
[62] D. Wang, Q. Sun, M.J. Hokkanen, C. Zhang, F.-Y. Lin, Q. Liu, S.-P. Zhu, T. Zhou, Q. Chang, B. He, Design of robust superhydrophobic surfaces, Nature 582 (2020) 55–59.
[63] S. Pan, R. Guo, M. Björnmalm, J.J. Richardson, L. Li, C. Peng, N. Bertleff-Zieschang, W. Xu, J. Jiang, F. Caruso, Coatings super-repellent to ultralow surface tension liquids, Nat. Mater. 17 (2018) 1040–1047.